



**Thank you for downloading this document from the RMIT Research Repository.**

The RMIT Research Repository is an open access database showcasing the research outputs of RMIT University researchers.

RMIT Research Repository: <http://researchbank.rmit.edu.au/>

**Citation:**

Ou, J, Ge, W, Carey, B, Daeneke, T, Rotbart, A, Shan, W, Wang, Y, Fu, Z, Chrimes, A, Wlodarski, W, Russo, S, Li, Y and Kalantar Zadeh, K 2015, 'Physisorption-based charge transfer in two-dimensional SnS<sub>2</sub> for selective and reversible NO<sub>2</sub> gas sensing', ACS Nano, vol. 9, no. 10, pp. 10313-10323.

**See this record in the RMIT Research Repository at:**

<https://researchbank.rmit.edu.au/view/rmit:34288>

**Version:** Accepted Manuscript

**Copyright Statement:**

© 2015 American Chemical Society

**Link to Published Version:**

<https://dx.doi.org/10.1021/acsnano.5b04343>

**PLEASE DO NOT REMOVE THIS PAGE**

# Physisorption Based Charge Transfer in Two-Dimensional SnS<sub>2</sub> for Selective and Reversible NO<sub>2</sub> Gas Sensing

Jian Zhen Ou,<sup>a,\*</sup> Wanyin Ge,<sup>b</sup> Benjamin Carey,<sup>a</sup> Torben Daeneke,<sup>a</sup> Asaf Rotbart,<sup>a</sup> Wei Shan,<sup>b</sup>  
Yichao Wang,<sup>a</sup> Zhengqian Fu,<sup>c</sup> Adam F. Chrimes,<sup>a</sup> Wojtek Wlodarski,<sup>a</sup> Salvy P. Russo,<sup>d,\*</sup> Yong  
Xiang Li,<sup>a-c,\*</sup> and Kourosch Kalantar-zadeh<sup>a,\*</sup>

<sup>a</sup> School of Electrical and Computer Engineering, RMIT University, Melbourne, Australia

<sup>b</sup> The Key Laboratory of Inorganic Functional Materials and Devices, Shanghai Institute of  
Ceramics, Chinese Academy of Sciences, Shanghai, P.R. China

<sup>c</sup> School of Physical Science and Technology, ShanghaiTech University, Shanghai, P.R. China

<sup>d</sup> School of Applied Sciences, RMIT University, Melbourne, Australia

Address correspondence to: J. Z. O (jianzhen.ou@rmit.edu.au), S. P. R  
(slavy.russo@rmit.edu.au), Y. L (yongxiang.li@rmit.edu.au) or K. K  
(kourosch.kalantar@rmit.edu.au).

## ABSTRACT

Nitrogen dioxide (NO<sub>2</sub>) is a gas species that plays an important role in certain industrial, farming and healthcare sectors. However, there are still significant challenges for NO<sub>2</sub> sensing at low detection limits, especially in the presence of other interfering gases. The NO<sub>2</sub> selectivity of current gas sensing technologies is significantly traded-off with their sensitivity and reversibility as well as fabrication and operating costs. In this work, we present an important progress for selective and reversible NO<sub>2</sub> sensing by demonstrating an economical sensing platform based on the charge transfer between physisorbed NO<sub>2</sub> gas molecules and two-dimensional (2D) tin disulfide (SnS<sub>2</sub>) flakes at low operating temperatures. The device shows high sensitivity and superior selectivity to NO<sub>2</sub> at operating temperatures of less than 160°C which are well below those of chemisorptive and ion conductive NO<sub>2</sub> sensors with much poorer selectivity. At the same time, excellent reversibility of the sensor is demonstrated which has rarely been observed in other 2D material counterparts. Such impressive features originate from the planar morphology of 2D SnS<sub>2</sub> as well as unique physical affinity and favorable electronic band positions of this material that facilitate the NO<sub>2</sub> physisorption and charge transfer at parts per billion (ppb) levels. The 2D SnS<sub>2</sub> based sensor provides a real solution for low-cost and selective NO<sub>2</sub> gas sensing.

**KEYWORDS:** Two dimensional materials; post transition metal dichalcogenide; SnS<sub>2</sub>; gas sensor; nanosheet; physisorption

Nitrogen dioxide (NO<sub>2</sub>) is an industrially and biologically important gas species, which can be particularly dangerous to humans at levels greater than 1 parts per million (ppm), causing damage to the respiration system and worsening respiratory diseases.<sup>1, 2</sup> The US environmental protection agency recognizes NO<sub>2</sub> as an air pollutant that is co-released during many types of fuel combustions.<sup>3</sup> It plays an important role in the chemistry of the atmosphere producing acid rain and contributing to the formation of ozone (O<sub>3</sub>), which is the major cause of photochemical smog.<sup>4</sup> NO<sub>2</sub> is also an important material for the synthesis of nitric acid that is used in the production of fertilizers for agriculture and explosives for both military and mining uses.<sup>5</sup> Furthermore, NO<sub>2</sub> is an essential gas for many bio-systems. Nitrogen monoxide (NO) appears as a gasotransmitter in many cell signaling pathways,<sup>6</sup> which can convert to NO<sub>2</sub> rapidly when exposed to an environmental disturbance in the presence of oxygen. The sensing of nitrogen oxides (NO<sub>x</sub>, a group mainly consists of NO<sub>2</sub> and NO) can be potentially implemented in diagnostic processes. For instance, the detection of NO<sub>x</sub> in exhaled breath (at parts per billion (ppb) levels) is helpful for identifying infections of lung tissues.<sup>7</sup> In addition, the NO<sub>x</sub> can possibly be used as a biomarker for some of the gastrointestinal disorder symptoms such as irritable bowel disease.<sup>6</sup>

It is important to consider that in many of the aforementioned sensing scenarios, NO<sub>2</sub> gas should be measured in the presence of other interfering gas species. Therefore, the realization of accurate, highly selective and low detection limit NO<sub>2</sub> gas sensors, which can operate in a wide range of ambient conditions, is a critical step in environmental monitoring and surveillance in many industries as well as healthcare and clinical practices.

Based on the sensing mechanism, the current NO<sub>2</sub> gas sensor technologies can be mainly categorized into optical, electrochemical and chemiresistor types.<sup>8</sup> Optical methods predominately rely on the unique optical fingerprints of NO<sub>2</sub> gas molecules including their chemiluminescent emission and infrared light absorption wavelengths, which result in high selectivity NO<sub>2</sub> sensing. Such optical sensing methods need sophisticated instruments or system configurations to achieve a high NO<sub>2</sub> sensitivity, which significantly increase their sizes and costs.<sup>8-12</sup> Instead, electrochemical

sensing of NO<sub>2</sub>, which relies on the electrochemical reduction of NO<sub>2</sub> in the presence of noble catalysts, is a low-cost approach.<sup>13</sup> Nevertheless, such sensors have cross-talk with active gas species such as hydrogen and their operation lifetime are relatively short.<sup>14</sup> These drawbacks can be increasingly eliminated by using zirconia-based solid electrolytes.<sup>15</sup> However, their high operation temperatures (in the range of 500-900 °C) result in significant operation costs and limit their applications mostly to combustion and automotive monitoring systems. Another economical method of NO<sub>2</sub> sensing is based on chemiresistor transducing platforms, relying on the charge transfer between metal oxides and surface chemisorbed NO<sub>2</sub>.<sup>16, 17</sup> However, the pristine or modified surface of these metal oxides shows weak discrimination to different gas species, making them poorly selective. Furthermore, the presence of oxygen is crucial for the operation of chemiresistive metal oxide compounds, which is not suitable for some particular anaerobic applications. Finally high operation temperature of above 200°C is needed in order to improve the response and recovery kinetics of these sensors.

Therefore, considering the trade-offs between sensitivity, selectivity and cost, there still exists an on-going quest for the ideal NO<sub>2</sub> sensing platform. The paramagnetic nature of NO<sub>2</sub> can be utilized to realize a different class of highly selective NO<sub>2</sub> gas sensors, as it can produce a magnetic dipole in addition to a surface electric dipole generated by the mirror charge when it is physisorbed onto the surface of a sensitive layer, resulting in a much stronger affinity compared to other non-magnetic gases such as CO<sub>2</sub>, H<sub>2</sub>, H<sub>2</sub>S and CH<sub>4</sub>.<sup>18</sup> Upon the NO<sub>2</sub> molecule adsorption, a charge transfer can occur depending on the relative band positions of sensitive material and NO<sub>2</sub> as well as possible hybridization of gas molecule states with sensitive material orbitals.<sup>19, 20</sup> Such a charge transfer affects the electrical resistance of the sensitive material, which can be easily measured using the low-cost resistive transducing platform. More importantly, the physisorption of gas molecules can be occurred at low temperatures and the corresponding charge transfer mechanism does not rely on the breakdown of the adsorbed gas, presenting an ideal NO<sub>2</sub> sensing platform that can operate reliably at relatively low temperatures, regardless of the presence of ambient oxygen.

So far, the search for exploring suitable sensitive materials for selective NO<sub>2</sub> physisorptive sensing with high adsorption/desorption kinetics has resulted in limited success. Low-dimensional carbon-based materials, including carbon nanotube and graphene, have been investigated as possible candidates.<sup>21-24</sup> Although excellent sensitivities toward NO<sub>2</sub> have been demonstrated, these sensors exhibit low selectivity and slow recovery kinetics.<sup>25</sup> The emergence of two-dimensional (2D) transition metal dichalcogenides (TMDs)<sup>26-30</sup> and phosphorene<sup>31, 32</sup> as the alternatives have alleviated some of these drawbacks but the outcomes are still far from sufficient practical values. Especially the most prominent candidate to date, 2D molybdenum disulfide (MoS<sub>2</sub>), despite presenting a good selectivity to NO<sub>2</sub> it does not show sufficiently fast recovery kinetics. Therefore, the realization of a low-cost sensing platform with strong potentials of excellent NO<sub>2</sub> physisorptive selectivity, sensitivity and reversibility, which can operate at relatively low temperatures at a small development cost, is pending to the discovery of an appropriate candidate material with a favorable surface energy value for NO<sub>2</sub> adsorption as well as optimum electronic band structure facilitating the charge transfer.

Although tin (Sn) does not belong to the transition metal family, tin disulfide (SnS<sub>2</sub>) exists in a layered crystal phase,<sup>33</sup> which is similar to TMDs in various aspects.<sup>34, 35</sup> This phase is composed of Sn atoms sandwiched between two layers of hexagonally disposed close packed sulfur (S) atoms, the adjacent S layers are connected by the weak van der Waal's forces (Figure 1a). Compared to 2D MoS<sub>2</sub>, SnS<sub>2</sub> has a larger electronegativity, potentially enhancing gas adsorption sites.<sup>36</sup> Furthermore, the relatively stronger temperature dependency on the electronic band structure of SnS<sub>2</sub> can possibly enable the optimization of sensing response and be used for enhancing recovery kinetics at a range of moderately elevated temperatures, advantageous for practical gas sensing applications.<sup>37,</sup>

38

In this work, we present a novel approach for selective and reversible NO<sub>2</sub> gas sensing based on 2D SnS<sub>2</sub> flakes. Many of the current synthesis methods of 2D SnS<sub>2</sub> are based on exfoliation, wet chemical and vapor deposition techniques.<sup>39-45</sup> Here, the planar 2D SnS<sub>2</sub> flakes are synthesized *via* a

facile wet chemical route. The planar few-layered 2D structure is selected as it both provides large active surface area for more efficient adsorption of NO<sub>2</sub> gas molecules and also facilitates their accommodation into the van der Waal' spacing due to small SnS<sub>2</sub> interlayer binding energy (~10-20 meV/Å<sup>2</sup>).<sup>46</sup> We shows that these 2D SnS<sub>2</sub> flakes are integrated onto low-cost resistive transducing platforms for highly selective and excellent sensitive NO<sub>2</sub> gas sensing at ppb levels, which relies on the physisorption based charge transfer.

## RESULTS AND DISCUSSION

The 2D SnS<sub>2</sub> flakes were prepared by a wet chemical synthesis technique (details are presented in Materials and Method section). In brief, upon the mixture of Sn precursor and sulfurization reagents at elevated temperatures, the preferential crystal nucleation occurs at the lateral planes due to the strong coupling along them. The existence of excessive dangling bonds at the edges causes the growth of SnS<sub>2</sub> crystals to be continued with a high anisotropic nature, resulting in the planar 2D morphology. Atomic force microscopy (AFM) verifies the presence of 2D hexagonal flakes with the thicknesses in the order of multiple SnS<sub>2</sub> unit cells in the as-synthesized flakes. A typical example is the AFM image shown in Figure 1b, which is a ~6 nm thick 2D flake corresponding to 10 monolayers of SnS<sub>2</sub>, as the thickness of a monolayer SnS<sub>2</sub> is ~0.59 nm.<sup>39, 41</sup> [ENREF 35](#) A statistical analysis based on AFM measurements indicates that the 2D flakes have different thicknesses with the majority lying in the range of 7 to 11 monolayers (Figure S1a). The obtained hexagonal 2D flakes demonstrate some polydispersity in lateral dimensions mainly ranging from 80 to 200 nm according to the transmission electron microscopy (TEM) imaging and dynamic light scattering (DLS) pattern shown in Figures 1c and S1b, respectively. Figure 1d shows the high resolution TEM (HRTEM) image of a 2D SnS<sub>2</sub> flake, in which a lattice fringe spacing of 0.319 nm is identified and corresponds to both the ( $\bar{1}100$ ) and (01 $\bar{1}0$ ) lattice planes of hexagonal SnS<sub>2</sub>. The inset in Figure 1d presents the fast Fourier transform (FFT) pattern of this region, showing the faceted edges with an angle of 120°, which corresponds to the hexagonal symmetry of crystalline

SnS<sub>2</sub> projected along the *c*-axis. The cross-sectional HRTEM image illustrated in Figure 1e confirms that these 2D SnS<sub>2</sub> flakes consist of average  $9 \pm 2$  layers with the interlayer distance of 0.587 nm (Figure 1f).

X-ray diffraction (XRD) assessment was utilized to further investigate the crystal phase of 2D hexagonal SnS<sub>2</sub> flakes. From Figure 2a, the primary diffraction peaks of 2D flakes at 15.04°, 28.27°, 32.17°, 41.95°, 50.05°, 52.45° and 60.62° are ascribed to the (001), (100), (101), (102), (110), (111), (201) planes, respectively, which are in accordance with hexagonal 2H SnS<sub>2</sub> structure (ICDD 23-0677). 2H SnS<sub>2</sub> belongs to space group of  $P\bar{3}m1$  and has three atoms in the unit cell, which extends over only one monolayer.<sup>47</sup> However, the additional appearance of a small diffraction peak at ~58° and the relatively intensified peak at 50.05° suggest the co-existence of another SnS<sub>2</sub> crystal phase, which can be identified as 4H structure (ICDD 21-1231). Although it is still within the hexagonal domain, the space group of 4H SnS<sub>2</sub> is changed to  $P6_3mc$ , which contains six atoms in a single unit cell and extends over two monolayers.<sup>47</sup> It is found that its composition is almost equal to that of 2H phase when the reaction time is shortened (Figure S2), suggesting that this additional phase might be an intermediate phase during the chemical reaction.

The concurrent phase phenomenon can also be investigated by Raman spectroscopy. From Figure 2b, two distinguished Raman peaks can be found at ~205 and ~314 cm<sup>-1</sup> and there is a broad peak centered at ~288 cm<sup>-1</sup> for the 2D SnS<sub>2</sub> flakes. The 314 cm<sup>-1</sup> peak can be ascribed to the vertical plane vibration mode ( $A_{1g}$ ) of Sn–S bonds of 2H SnS<sub>2</sub>.<sup>39, 47</sup> Nevertheless, this peak can also be contributed to the  $A_1+E$  vertical vibration Raman mode of 4H structure due to the close position between these two structures (~313.5 cm<sup>-1</sup> for 4H structure vs. ~314 cm<sup>-1</sup> for 2H structure<sup>39, 47</sup>). Instead, the in-plane vibrational  $E$  mode allows a facile discrimination between 2H and 4H structures. The  $E_g$  mode of 2H structure appears as a single and intense band at 205 cm<sup>-1</sup>, whereas the  $E$  mode of 4H structure gives rise to a doublet at 200 and 214 cm<sup>-1</sup> according to previous literature.<sup>39, 47</sup> Therefore, the composition of 4H structure in the 2D SnS<sub>2</sub> flakes is minor. The broad peak centered at 288 cm<sup>-1</sup> may also be ascribed to the  $A_{1g}$  Raman mode of 2H SnS<sub>2</sub> as a previous



report shows that it is merged in the prominent  $A_{1g}$  mode centered at  $314\text{ cm}^{-1}$ .<sup>39</sup> However, the position of this peak is overlapped with that of  $B_{2g}$  Raman mode of SnS.<sup>48, 49</sup> The XPS results in Figure S3a show that there is no  $\text{Sn}^{2+}$  signature in the 2D  $\text{SnS}_2$  flakes, indicating that the amount of SnS in the flake is negligible.

The optical properties of the 2D flakes were studied by measuring their absorption spectrum (Figure 2c). An absorption peak at  $\sim 580\text{ nm}$  with the shoulder centered at  $\sim 660\text{ nm}$  can be observed, which are ascribed to the indirect excitonic transition from  $\Gamma$  to M point of the Brillouin zone in 2H and 4H  $\text{SnS}_2$  structures, respectively.<sup>50</sup> The broad peak centered at  $\sim 490\text{ nm}$  can be the convoluted peak of the direct excitonic transition at the M point for both 2H and 4H structures according to a previous measurement ( $\sim 484\text{ nm}$  for 2H and  $\sim 510\text{ nm}$  for 4H)<sup>51</sup> and theoretical calculation values ( $\sim 443\text{ nm}$  for 2H and  $\sim 454\text{ nm}$  for 4H).<sup>50</sup> The corresponding photoluminescence (PL) spectrum of 2D  $\text{SnS}_2$  flakes was investigated at the excitation wavelength of  $532\text{ nm}$ . From Figure 2d, a relatively sharp peak at  $\sim 580\text{ nm}$  is observed, which is consistent with the position of indirect excitonic peak of 2H  $\text{SnS}_2$ . It should be noted that the position is also close to that of  $\text{SnO}_x$ .<sup>52</sup> However, the XPS analysis presented in Figure S3 indicates that there is no observable co-existing  $\text{SnO}_x$  in the 2D  $\text{SnS}_2$  flakes. The broad peak centered at  $\sim 660\text{ nm}$  can be ascribed to the hot PL of the indirect exciton recombination of 4H  $\text{SnS}_2$ . Although such a broad peak has been ascribed to the PL originated from the structural impurities by a number of researchers,<sup>53, 54</sup> the energy dispersive X-ray (EDX) survey spectrum in Figure S4a together with the XRD pattern in Figure 2a show no observable structural impurities in 2D  $\text{SnS}_2$  flakes. In addition, the measured Sn/S composition ratio is  $\sim 1:2$ , matching the theoretical value of  $\text{SnS}_2$ , implying that the influence of substoichiometric levels and sulfur vacancies toward the electronic and optical properties of the flakes can be neglected. The mapping images of Sn and S elements displayed in Figure S4b demonstrate that both Sn and S distribute uniformly along the flake.

The 2D  $\text{SnS}_2$  gas sensors were fabricated by drop-casting of the solution containing 2D  $\text{SnS}_2$  flakes on the resistive transducing substrates which were made of alumina with surface

interdigitated electrode (IDE) patterns (Specification was presented in Materials and Method section). The IDE metal is chosen to assure that Ohmic contacts were formed with drop-casted SnS<sub>2</sub>. The electrical resistance of the device was measured for calculating the gas response factor using  $R_g/R_a$  for  $R_g > R_a$ , or  $R_a/R_g$  for  $R_g < R_a$ , where  $R_a$  and  $R_g$  represent the resistance of the device to air and the analyte gas, respectively. The sensor response and recovery time are defined as the time required for a 90% change in the full magnitude change of the gas response factor.

We tested the operation temperature of sensors from room to 160°C. For the temperatures lower than 80°C, the device did not show acceptable response/recovery time and additionally  $R_g$  was relatively large and beyond the measurement range of the Ohm-meter. There is an observable transition from SnS<sub>2</sub> to tin oxide compounds (SnO<sub>x</sub>) when the operation temperature exceeds 160°C (Figure S5) and therefore operation at such elevated temperatures is ruled out.

From Figure 3a and Table S1, after the exposure to 10 ppm NO<sub>2</sub> in synthetic air balance at the operation temperature of 80°C, the sensor's resistance is impressively ~28 times larger than that of only synthetic air (translates into the initial response factor of ~28). As will be fully discussed later, the surface adsorbed NO<sub>2</sub> gas molecules act as electron acceptors to receive electrons from 2D SnS<sub>2</sub> flakes. Such charge transfers reduce the number of free electrons in the flakes, increasing the resistance. With the increase of the operating temperature, the response factor is enhanced while the response and recovery time are decreased, suggesting that the increase of the temperature facilitates the adsorption of NO<sub>2</sub> gas molecules onto the 2D SnS<sub>2</sub> surface and enhances the charge transfer. The optimal sensing takes place at 120°C with a maximum response factor of ~36 with the shortest response and recovery time of ~170 and ~140 s, respectively. By further increasing the operating temperature beyond 120°C, the response factor is dramatically dropped and the response time is slightly increased, implying that the surface desorption process of NO<sub>2</sub> gas becomes a more dominant effect at such temperatures.

The dynamic performance of the sensor towards NO<sub>2</sub> gas with concentrations ranged from 0.6 to 10 ppm at the optimum operation temperature of 120°C was shown in Figure 3b. With the increase

in the concentration of NO<sub>2</sub>, more surface dipoles are formed before the NO<sub>2</sub> coverage reaches its maximum, resulting in more electron transfer from SnS<sub>2</sub> to NO<sub>2</sub>. The measured response factor of the sensor is observed to be almost linear with the exposure concentrations of NO<sub>2</sub> gas, while the response time is greatly decreased when increasing the NO<sub>2</sub> concentration from 0.6 to 1.2 ppm and reaches the saturation stage afterwards (Table S2). Excellent sensor reversibility is observed (Figure 3b and Figure S6) with the recovery time of less than 180 s at the optimum operating temperature regardless of the NO<sub>2</sub> concentration. This remarkable reversibility is not commonly seen in physisorptive charge transfer based sensors and the recovery time of such systems can be up to several orders of magnitude longer due to their slow recovery kinetics.<sup>22</sup> Based on the NO<sub>2</sub> dynamic responses, the NO<sub>2</sub> detection limit of our sensor is estimated to be ~20-30 ppb at a noise level of ±5%. Such a low detection limit is superior in comparison to those of low-cost NO<sub>2</sub> optical and electrochemical sensors, which are both only in the ppm ranges<sup>9, 12, 13, 15</sup> and comparable to those of best-reported metal oxide based chemisorptive gas sensors (10-50 ppb)<sup>16</sup> which are not NO<sub>2</sub> selective. The value is also close to those of 2D MoS<sub>2</sub><sup>28</sup> and carbon<sup>22</sup> based physisorptive gas sensors which show poor reversibility.

The 2D SnS<sub>2</sub> flakes are very strongly selective to NO<sub>2</sub> as only minimal responses toward other gases under investigation in this work are observed. At 120°C, which is the near optimal operating temperature for all those gases, response factors at industrially meaningful concentrations for H<sub>2</sub> (1%), CH<sub>4</sub> (10%), CO<sub>2</sub> (10%) and H<sub>2</sub>S (56 ppm) are found to be ~1.0, ~1.1, ~1.1 and ~1.3, respectively, in comparison to ~36 for NO<sub>2</sub> (10 ppm) (Figure 3c). The particular selected concentrations of toxic NO<sub>2</sub> (10 ppm) and H<sub>2</sub>S (56 ppm) gases are well below the immediately dangerous to life or health (IDLH) values defined by US national institute for occupational safety and health (NIOSH), which are 20 and 100 ppm, respectively.<sup>55</sup> The exposure limit of NO<sub>2</sub> defined by NIOSH is recommended to be 1 ppm.<sup>55</sup> If taking this into account, the NO<sub>2</sub> selectivity of this sensor is still superior as its response factor is ~10 at 1.2 ppm NO<sub>2</sub> which is almost an order magnitude higher than other aforementioned gases. In addition, the humidity plays a negligible role

in the NO<sub>2</sub> gas sensing performance of the sensor (Figure S7). It has also been previously shown that the response of nanostructured SnS<sub>2</sub> towards several other gases are relatively smaller than that of shown to NO<sub>2</sub> here. For instance, NH<sub>3</sub> has only a response of ~1.5 at a concentration of 100 ppm.<sup>56</sup>

To understand the selectivity of 2D SnS<sub>2</sub> flakes toward NO<sub>2</sub> gas, we calculated the molecule-surface binding energies using density functional theory (DFT) to assess the dispersion forces. The outcomes are shown in Figure 3d and Table S3. The closest distance between the molecules and the surface, for the bound gas species, range from 2.17 to 2.87 Å which is within the typical range for physisorbed molecules. The values of the binding energies also indicate the physisorption occurs between the molecule and the surface for CH<sub>4</sub>, CO<sub>2</sub>, H<sub>2</sub>S, NH<sub>3</sub> and NO<sub>2</sub>, with NO<sub>2</sub> being the most strongly bound species. The binding energy for NO<sub>2</sub> is approximately 140 meV greater than that of the next most bound species (NH<sub>3</sub>), while H<sub>2</sub> and O<sub>2</sub> are non-binding due to its small adsorption energy (~50 meV) and positive adsorption energy (Table S3), respectively. The repelling of O<sub>2</sub> molecules on the SnS<sub>2</sub> surface possibly indicates that the charge transfer to the physisorbed NO<sub>2</sub> molecules does not rely on the presence of O<sub>2</sub> gas, which is distinctly different from those of metal oxides based chemisorptive NO<sub>2</sub> sensors.<sup>16, 17</sup> The calculated surface binding energies toward different gas molecules are in accordance with the measurement results, confirming that the impressive selective NO<sub>2</sub> gas response of 2D SnS<sub>2</sub> flakes originates from its unique physical surface affinity to the gas molecules.

Another possible reason can be attributed to the influence of different gas molecules on SnS<sub>2</sub> electronic band structure. Figure 4 shows the spin resolved electronic Density of States (eDOS) plots for the clean SnS<sub>2</sub> surface and for surfaces onto which aforementioned gas molecules are physisorbed. For the most weakly bound gas species (CO<sub>2</sub> and CH<sub>4</sub>), the total eDOS and the projected eDOS of the nearest neighbor surface S atoms are almost the same as for the clean surface near the Fermi level, suggesting there is negligible charge transfer between the molecules and surface. The next most bound species, H<sub>2</sub>S and NH<sub>3</sub>, display similar features in the eDOS. In both

cases, molecular physisorption introduces states in the gap, and the projected eDOS indicates that both molecule and surface atom states contribute to this state in the band gap. In addition, the bands near the valance band maximum (VBM) is shifted down by nearly 0.1 eV compared to that of clean surface. However, these generated gap states are relatively far away from the Fermi level ( $\sim 0.5$ -1 eV), resulting in inefficient charge transfer between the physisorbed gas molecules and SnS<sub>2</sub> surface. In contrast, the eDOS for NO<sub>2</sub> physisorption is different from the other species. Firstly, the DOS is asymmetric when comparing spin-up and spin-down, possibly due to the formation of surface magnetic moment upon the physisorption of NO<sub>2</sub> gas molecules. More importantly, while the energy bands near the conduction band minimum (CBM) are lowered by  $\sim 60$  meV, the band states close to the Fermi level are raised in energy by approximately 20 meV compared to the clean surface, indicating significant charge transfer from SnS<sub>2</sub> to the physisorbed NO<sub>2</sub> gas molecules.

In comparison to other 2D semiconductors, it is noted that the response factor of 2D SnS<sub>2</sub> toward NO<sub>2</sub> is at least one order larger than that of exfoliated 2D MoS<sub>2</sub> at similar exposure concentration and operation temperature.<sup>28</sup> This can be mainly ascribed to the larger NO<sub>2</sub> adsorption energy of SnS<sub>2</sub> compared to MoS<sub>2</sub> ( $\sim 150$  meV),<sup>57</sup> resulting in more adsorption of NO<sub>2</sub> gas molecules either on the surface or possibly within the van der Waal's gap of SnS<sub>2</sub> through efficient intercalation as few-layered SnS<sub>2</sub> has a much weaker interlayer binding energy than that of MoS<sub>2</sub>.<sup>46</sup> In addition, the Mulliken population analysis of the charge density for the NO<sub>2</sub> physisorption indicates a transfer in charge density of  $0.048 e^-$  from SnS<sub>2</sub> surface to the NO<sub>2</sub> molecule, while only  $0.034 e^-$  is observed for that of MoS<sub>2</sub>.<sup>57</sup> Such an improvement can be possibly due to a more favorable Fermi energy of SnS<sub>2</sub> related to partially occupied molecular orbitals (POMO) of NO<sub>2</sub> (Figure 4), which is also another key factor for the strength of physisorption based charge transfer.

We observed that our 2D SnS<sub>2</sub> sensor demonstrates a much higher rate of NO<sub>2</sub> recovery kinetics compared to those of previously physisorption based sensors made of 2D materials (*e.g.* 2D MoS<sub>2</sub>) at elevated temperatures.<sup>26-28</sup> It is found that NO<sub>2</sub> gas molecules are favorably absorbed on the S atoms of SnS<sub>2</sub> with a calculated bond length of 2.41 Å, while the NO<sub>2</sub> gas molecules are adsorbed

onto Mo atoms of MoS<sub>2</sub> between two sandwiched S layers with a much shorter bond length of 1.21 Å.<sup>57</sup> Therefore, the thermal vibration energy available at an elevated temperature causes a more efficient NO<sub>2</sub> gas desorption from SnS<sub>2</sub> compared to MoS<sub>2</sub>. The stronger temperature dependence of SnS<sub>2</sub> Fermi level can also result in a more favorable position related to that of NO<sub>2</sub> POMO at elevated temperatures.<sup>37,38</sup> The temperature effect, together with its strong physical NO<sub>2</sub> affinity, ensures the domination of charge transfer from SnS<sub>2</sub> to NO<sub>2</sub> despite the large NO<sub>2</sub> gas desorption at relatively high temperatures.

The charge transfer phenomenon from the surface of 2D SnS<sub>2</sub> to the physisorbed NO<sub>2</sub> gas molecules is partially evidenced by Raman spectroscopy before and after the NO<sub>2</sub> exposure at 120°C. From Figure 5a, there is no observable Raman peak shift associated with stiffening, confirming no chemical bond modification upon the physisorption of NO<sub>2</sub> gas molecules. The intensity of A<sub>1g</sub> Raman mode is found to be significantly reduced, while the Raman E<sub>g</sub> mode seems to remain unchanged after the NO<sub>2</sub> exposure and their intensity ratio  $I(A_{1g}/E_g)$  is decreased from 1.05 to 0.8. The NO<sub>2</sub> adsorption may affect the equilibrium lattice parameter in SnS<sub>2</sub>. Additionally, the NO<sub>2</sub> molecules on the surface act as electron acceptors, modifying the electron-phonon interaction in SnS<sub>2</sub>. Similar to the cases of charge-transfer doping observed in graphene and TMDs,<sup>58-60</sup> such a modification leads to the phonon self-energy renormalization and consequently weakening of the phonons, causing the intensity decrease of the A<sub>1g</sub> mode that is more sensitive to the free electron density of the material.

The PL spectrum can be a good indicator in the charge transfer phenomenon as well. As SnS<sub>2</sub> is an *n*-type semiconductor,<sup>40</sup> its PL peak can be theoretically decomposed into the portions of neutral exciton and the negative trion.<sup>61</sup> A negative trion consists of two electrons to a hole, resulting in a negatively charged exciton, while the neutral exciton is coupled to the extra electron at the Fermi level.<sup>58</sup> Upon the adsorption of NO<sub>2</sub> gas molecules, the negative trion is converted back into the neutral exciton as the free electrons are depleted from SnS<sub>2</sub>. At the same time, the generated surface dipoles between the gas molecules and SnS<sub>2</sub> surface are strong enough to split the neutral excitons,

leading to a significant reduction in their recombination and subsequently a strongly quenched PL (Figure 5b), which is analogous to the PL modulation in MoS<sub>2</sub>-WS<sub>2</sub> heterostacks or electrical gating of MoS<sub>2</sub>.<sup>61, 62</sup> In addition, it seems that such gas molecules induced charge transfers show no difference on the crystal polytypes of SnS<sub>2</sub> as the quenched degrees of the 2H and 4H PL peaks are similar.

## CONCLUSIONS

We successfully developed a novel gas sensor based on 2D SnS<sub>2</sub> flakes with a very strong selectivity to NO<sub>2</sub> molecules. The 2D SnS<sub>2</sub> flakes were synthesized using a facile wet chemical route with a great potential for production scalability. The 2D structure of SnS<sub>2</sub> hexagonal planes were made of a few layers of unit cell thickness, which provided plenty of room for NO<sub>2</sub> molecule adsorption either on the surface or in-between the van der Waals's spacings. The NO<sub>2</sub> adsorption mechanism was theoretically and experimentally shown to be dominated by physisorption with a concurrent charge transfer into 2D SnS<sub>2</sub> flakes that could occur at relatively low operating temperatures. Our theoretical calculations also suggested no oxygen was involved in the NO<sub>2</sub> adsorption/desorption process, possibly indicating the sensor could also operate in anaerobic environments. The best NO<sub>2</sub> gas sensing performance of 2D SnS<sub>2</sub> was achieved at the optimum temperature of 120°C, reaching the detection limits of <30 ppb and showing an impressive response factor of ~36 when exposed to a NO<sub>2</sub> concentration of 10 ppm. Excellent NO<sub>2</sub> selectivity was demonstrated with reference to other gas species, which had not been previously exhibited for NO<sub>2</sub> gas sensors that operate based on a physisorptive charge transfer mechanism. Such a unique selectivity was ascribed to the strong physical affinity of paramagnetic NO<sub>2</sub> gas molecules towards SnS<sub>2</sub> surfaces as well as the relatively favorable position between Fermi level of SnS<sub>2</sub> and NO<sub>2</sub> POMO. Our 2D SnS<sub>2</sub> based NO<sub>2</sub> gas sensor was also highly reversible, showing excellent recovery to the baseline in contrast to 2D TMDs, such as 2D MoS<sub>2</sub>.

The realization of the presented economical, exceptionally selective and highly sensitive NO<sub>2</sub> gas sensing platform, which operates at relatively low temperatures without the presence of oxygen, provides a feasible approach to allow high performance NO<sub>2</sub> sensing for a wide range of applications in environmental monitoring, industry, clinical practices and healthcare.

## MATERIALS AND METHODS

**Synthesis of 2D SnS<sub>2</sub> flakes:** Tin (IV) chloride (SnCl<sub>4</sub>•5H<sub>2</sub>O, >99.9%, Sigma Aldrich, 0.5 mM) was added to a mixture of 5 mL oleic acid (OAc, >90.0%, Sigma Aldrich) and 10 mL octadecene (ODE, >90.0%, Sigma Aldrich) in a 100 mL three-neck flask to produce tin precursor. A standard Schlenk line was used to protect the reaction from oxygen and moisture under a flow of high-purity N<sub>2</sub>. The mixed solution was degassed at 120°C for 1 h to remove the moisture and the oxygen. Subsequently, the solution was heated to 280°C within 15 min with a vigorous stir (700 rpm). Sulfide powder (1 mM) was dispersed into 5 mL oleylamine (OAm, >90.0%, Sigma Aldrich) to produce the sulfide precursor which was subsequently injected into the reaction system. The reaction was maintained at 280 °C for 30 min. After cooling the solution to room temperature, the 2D SnS<sub>2</sub> flakes (in powder form) were collected and separated from the solution by centrifugation. The powder was further washed two times by ethanol and hexane (1/1, V/V) and finally dispersed in ethanol. The powder was stable in air without further protection for characterizations.

**Morphological, structural and optical characterizations:** Lateral dimensions and thickness of 2D SnS<sub>2</sub> flakes were measured using DLS (ALV fast DLS particle sizing spectrometer) and AFM (Bruker Multimode 8 with PF TUNA), respectively. Their crystal structure was characterized using XRD (Philips PANalytical) with CuK $\alpha$  radiation at 45 kV and 40 mA, HRTEM (TEM, Tecnai F20, FEI) at an accelerating voltage of 200 kV and Raman spectroscopy (Craic 20-30 microspectrophotometer) under the excitation wavelength of 785 nm at 1 mW power. The EDX spectrum and mapping of the flakes were carried out by scanning electron microscopy (JEOL



JSM6700F) equipped with an EDX spectroscopy. The optical absorption spectra of the 2D flakes were examined using a Varian Cary 500 spectrometer in dual beam mode using quartz cuvettes. PL spectroscopy was carried out on a Princeton Instruments SP2500i with a PIXIS100 ExCelon CCD camera detector using a Monochromatic 532 nm laser delivering approximately 200  $\mu$ W average power to the sample.

***Gas sensor fabrication and characterization:*** The transducing substrates were made of alumina pattern with 8 pairs of IDE Pt electrodes. The spacing between each IDE pair was 200  $\mu$ m. 5  $\mu$ L of suspension containing 1 mg/mL 2D SnS<sub>2</sub> flakes was drop-casted on the transducing substrate within the exposed area of 0.5 cm  $\times$  0.5 cm at a temperature of 50°C. The resistance of the sensor was measured using Agilent 34410A digital multimeter. The gas sensing measurements were conducted in a LINKAM (Scientific Instruments) customized gas testing chamber with the capability to control the operation temperature for up to 600°C. A computerized mass flow control (MFC) multi-channel gas calibration system was used to regulate the incoming gas stream at a total constant flow rate of 200 standard cubic centimeters per minute (sccm) to the LINKAM chamber. For the investigation of NO<sub>2</sub> gas sensing performance in the humidified environment, the humidification of the gas was realized by a simple unheated bubble humidifier, in which the gas was forced down a tube into the bottom of a bottle containing 100 mL of water. The gas then escaped from the distal end of the tube under water surface forming bubbles, which gained humidity as they rose to the water surface. Given the relatively smaller gas flow rate (200 sccm or 0.2 L/min), the relative humidity (RH) of the incoming gas stream towards the sensor reached approximately 100%,<sup>63, 64</sup> which was also confirmed by a commercial humidity sensor.

***Theoretical calculation on the surface adsorption energy and total density of states:*** Spin-dependent Hybrid DFT calculations were carried out in Gaussian basis set *ab initio* package CRYSTAL14.<sup>65, 66</sup> The B3LYP hybrid exchange-correlation functional was used<sup>67</sup> that was augmented with an empirical London-type correction to the energy in order to incorporate dispersion contributions to the overall energy. The correction term used in these calculations is the

one proposed by Grimme,<sup>68</sup> which has been successfully used with B3LYP to calculate cohesive energies in dispersion bonded molecular crystals.<sup>69</sup> For all atoms (other than Sn) a triple zeta valence (TZV) basis set, with polarization functions, was used for modeling the electrons.<sup>70</sup> In contrast, a fully relativistic effective core potential was used for Sn, accounting for the 28 core electrons ( $1s^2 2s^2 2p^6 3s^2 3p^6 3d^{10}$ ) and a 411(51d) basis set for the valence electrons.<sup>71</sup> A periodic  $3 \times 3 \times 1$  or  $5 \times 5 \times 1$  slab of  $\text{SnS}_2$  was used for representing the  $\text{SnS}_2$  surface. Initially, each target gas molecule was placed  $\sim 1.5 \text{ \AA}$  from the S surface layer of  $\text{SnS}_2$  and the molecule/slab configuration was geometry optimized prior to calculating the molecule-slab binding energy.

## ACKNOWLEDGEMENT

The authors acknowledge support from the Australian Research Council (ARC) through Discovery Project DP140100170. The authors would also like to acknowledge the facilities as well as scientific and technical assistance of the Australian Microscopy & Microanalysis Research Facility at the RMIT University Microscopy & Microanalysis Facility, and the Micro Nano Research Facility (MNRF) at RMIT University. This work was also supported by the Chinese National Natural Science Foundation (51172257, 61371060), the CAS/SAFEA International Partnership Program for Creative Research Teams.

## SUPPORTING INFORMATION

AFM statistical analysis and DLS measurements of 2D  $\text{SnS}_2$  flakes; XRD pattern of flakes synthesized by shorter reaction time; XPS analysis of 2D  $\text{SnS}_2$  flakes; EDX spectrum and mapping of 2D  $\text{SnS}_2$  flakes; Raman spectra of 2D  $\text{SnS}_2$  flakes at different temperatures; The recovery kinetics of 2D  $\text{SnS}_2$  flakes after  $\text{NO}_2$  gas exposure;  $\text{NO}_2$  gas sensing performance of 2D  $\text{SnS}_2$  flakes in the humidified environment.

## REFERENCES

1. Guarnieri, M.; Balmes, J. R. Outdoor Air Pollution and Asthma. *Lancet* 2014, 383, 1581-1592.
2. Schwela, D. Air Pollution and Health in Urban Areas. *Rev. Environ. Health* 2000, 15, 13-42.
3. EPA, U. S. Air Pollution. [www.epa.gov/air/nitrogenoxides/](http://www.epa.gov/air/nitrogenoxides/) (accessed 30/06/2015).
4. Atkinson, R. Atmospheric Chemistry of VOCs and NO<sub>x</sub>. *Atmos. Environ.* 2000, 34, 2063-2101.
5. Hodge, C. A. *Pollution Control in Fertilizer Production*. CRC Press: 1994.
6. Ou, J. Z.; Yao, C.; Rotbart, A.; Muir, J. G.; Gibson, P. R.; Kalantar-zadeh, K. Human Intestinal Gas Measurement Systems: *In Vitro* Fermentation and Gas Capsules. *Trends in biotechnol.* 2015, 33, 208-213.
7. Puckett, J. L.; George, S. C. Partitioned Exhaled Nitric Oxide to Non-Invasively Assess Asthma. *Resp. Physiol. Neurobi.* 2008, 163, 166-177.
8. Andringa, A.-M.; Piliago, C.; Katsouras, I.; Blom, P. W. M.; Leeuw, D. M. d. NO<sub>2</sub> Detection and Real-Time Sensing with Field-Effect Transistors. *Chem. Mater.* 2014, 26, 773-785.
9. Swanson, J. J.; Watts, W. F.; Newman, R. A.; Ziebarth, R. R.; Kittelson, D. B. Simultaneous Reduction of Particulate Matter and NO<sub>x</sub> Emissions Using 4-Way Catalyzed Filtration Systems. *Environ. Sci. Technol.* 2013, 47, 4521-4527.
10. De Castro, A. J.; Meneses, J.; Briz, S.; López, F. Nondispersive Infrared Monitoring of NO Emissions in Exhaust Gases of Vehicles. *Rev. Sci. Instrum.* 1999, 70, 3156-3159.
11. Jimenez, J. L.; McRae, G. J.; Nelson, D. D.; Zahniser, M. S.; Kolb, C. E. Remote Sensing of NO and NO<sub>2</sub> Emissions from Heavy-Duty Diesel Trucks Using Tunable Diode Lasers. *Environ. Sci. Technol.* 2000, 34, 2380-2387.

12. Wang, X.-D.; Wolfbeis, O. S. Fiber-Optic Chemical Sensors and Biosensors. *Anal. Chem.* 2013, 85, 487-508.
13. Chang, S.-C.; Stetter, J. R. Electrochemical NO<sub>2</sub> Gas Sensors: Model and Mechanism for the Electroreduction of NO<sub>2</sub>. *Electroanal.* 1990, 2, 359-365.
14. Privett, B. J.; Shin, J. H.; Schoenfisch, M. H. Electrochemical Sensors. *Anal. chem.* 2008, 80, 4499-4517.
15. Zhuiykov, S.; Miura, N. Development of Zirconia-Based Potentiometric NO<sub>x</sub> Sensors for Automotive and Energy Industries in the Early 21st Century: What are the Prospects for Sensors? *Sensor Actuat. B-Chem.* 2007, 121, 639-651.
16. Afzal, A.; Cioffi, N.; Sabbatini, L.; Torsi, L. NO<sub>x</sub> Sensors based on Semiconducting Metal Oxide Nanostructures: Progress and Perspectives. *Sensor Actuat. B-Chem.* 2012, 171–172, 25-42.
17. Fine, G. F.; Cavanagh, L. M.; Afonja, A.; Binions, R. Metal Oxide Semiconductor Gas Sensors in Environmental Monitoring. *Sensors* 2010, 10, 5469.
18. Wehling, T. O.; Novoselov, K. S.; Morozov, S. V.; Vdovin, E. E.; Katsnelson, M. I.; Geim, A. K.; Lichtenstein, A. I. Molecular Doping of Graphene. *Nano Lett.* 2008, 8, 173-177.
19. Leenaerts, O.; Partoens, B.; Peeters, F. M. Adsorption of H<sub>2</sub>O, NH<sub>3</sub>, CO, NO<sub>2</sub>, and NO on Graphene: A First-Principles Study. *Phys. Rev. B* 2008, 77, 125416.
20. Hu, T.; Gerber, I. C. Theoretical Study of the Interaction of Electron Donor and Acceptor Molecules with Graphene. *J. Phys. Chem. C* 2013, 117, 2411-2420.
21. Llobet, E. Gas Sensors Using Carbon Nanomaterials: A Review. *Sensor Actuat. B-Chem.* 2013, 179, 32-45.
22. Iqbal, N.; Afzal, A.; Cioffi, N.; Sabbatini, L.; Torsi, L. NO<sub>x</sub> Sensing One- and Two-Dimensional Carbon Nanostructures and Nanohybrids: Progress and Perspectives. *Sensor Actuat. B-Chem.* 2013, 181, 9-21.

23. Li, H.; Wu, J.; Qi, X.; He, Q.; Liusman, C.; Lu, G.; Zhou, X.; Zhang, H. Graphene Oxide Scrolls on Hydrophobic Substrates Fabricated by Molecular Combing and Their Application in Gas Sensing. *Small* 2013, 9, 382-386.
24. He, Q.; Wu, S.; Yin, Z.; Zhang, H. Graphene-based Electronic Sensors. *Chem. Sci.* 2012, 3, 1764-1772.
25. Schedin, F.; Geim, A. K.; Morozov, S. V.; Hill, E. W.; Blake, P.; Katsnelson, M. I.; Novoselov, K. S. Detection of Individual Gas Molecules Adsorbed on Graphene. *Nat. Mater.* 2007, 6, 652-655.
26. Cho, B.; Hahm, M. G.; Choi, M.; Yoon, J.; Kim, A. R.; Lee, Y.-J.; Park, S.-G.; Kwon, J.-D.; Kim, C. S.; Song, M., *et al.* Charge-Transfer-Based Gas Sensing Using Atomic-Layer MoS<sub>2</sub>. *Sci. Rep.* 2015, 5, 8052.
27. Late, D. J.; Huang, Y.-K.; Liu, B.; Acharya, J.; Shirodkar, S. N.; Luo, J.; Yan, A.; Charles, D.; Waghmare, U. V.; Dravid, V. P., *et al.* Sensing Behavior of Atomically Thin-Layered MoS<sub>2</sub> Transistors. *ACS Nano* 2013, 7, 4879-4891.
28. Donarelli, M.; Prezioso, S.; Perrozzi, F.; Bisti, F.; Nardone, M.; Giancaterini, L.; Cantalini, C.; Ottaviano, L. Response to NO<sub>2</sub> and Other Gases of Resistive Chemically Exfoliated MoS<sub>2</sub>-Based Gas Sensors. *Sensor Actuat. B-Chem.* 2015, 207, 602-613.
29. He, Q.; Zeng, Z.; Yin, Z.; Li, H.; Wu, S.; Huang, X.; Zhang, H. Fabrication of Flexible MoS<sub>2</sub> Thin-Film Transistor Arrays for Practical Gas-Sensing Applications. *Small* 2012, 8, 2994-2999.
30. Li, H.; Yin, Z.; He, Q.; Li, H.; Huang, X.; Lu, G.; Fam, D. W. H.; Tok, A. I. Y.; Zhang, Q.; Zhang, H. Fabrication of Single- and Multilayer MoS<sub>2</sub> Film-Based Field-Effect Transistors for Sensing NO at Room Temperature. *Small* 2012, 8, 63-67.

31. Abbas, A. N.; Liu, B.; Chen, L.; Ma, Y.; Cong, S.; Aroonyadet, N.; Köpf, M.; Nilges, T.; Zhou, C. Black Phosphorus Gas Sensors. *ACS Nano* 2015, 9, 5618-5624.
32. Kou, L.; Frauenheim, T.; Chen, C. Phosphorene as a Superior Gas Sensor: Selective Adsorption and Distinct  $I-V$  Response. *J. Phys. Chem. Lett.* 2014, 5, 2675-2681.
33. Julien, C.; Eddrief, M.; Samaras, I.; Balkanski, M. Optical and Electrical Characterizations of SnSe, SnS<sub>2</sub> and SnSe<sub>2</sub> Single Crystals. *Mat. Sci. Eng. B-Solid* 1992, 15, 70-72.
34. Chhowalla, M.; Shin, H. S.; Eda, G.; Li, L. J.; Loh, K. P.; Zhang, H. The Chemistry of Two-Dimensional Layered Transition Metal Dichalcogenide Nanosheets. *Nat. Chem.* 2013, 5, 263-275.
35. Varrla, E.; Backes, C.; Paton, K. R.; Harvey, A.; Gholamvand, Z.; McCauley, J.; Coleman, J. N. Large-Scale Production of Size-Controlled MoS<sub>2</sub> Nanosheets by Shear Exfoliation. *Chem. Mater.* 2015, 27, 1129-1139.
36. Xu, Y.; Schoonen, M. A. A. The Absolute Energy Positions of Conduction and Valence Bands of Selected Semiconducting Minerals. *Am. Mineral.* 2000, 85, 543-556.
37. Patil, S. G.; Tredgold, R. H. Electrical and Photoconductive Properties of SnS<sub>2</sub> Crystals. *J. Phys. D Appl. Phys.* 1971, 4, 718.
38. El-Mahalawy, S. H.; Evans, B. L. Temperature Dependence of the Electrical Conductivity and Hall Coefficient in 2H-MoS<sub>2</sub>, MoSe<sub>2</sub>, WSe<sub>2</sub>, and MoTe<sub>2</sub>. *physica status solidi B* 1977, 79, 713-722.
39. Huang, Y.; Sutter, E.; Sadowski, J. T.; Cotlet, M.; Monti, O. L. A.; Racke, D. A.; Neupane, M. R.; Wickramaratne, D.; Lake, R. K.; Parkinson, B. A., *et al.* Tin Disulfide—An Emerging Layered Metal Dichalcogenide Semiconductor: Materials Properties and Device Characteristics. *ACS Nano* 2014, 8, 10743-10755.

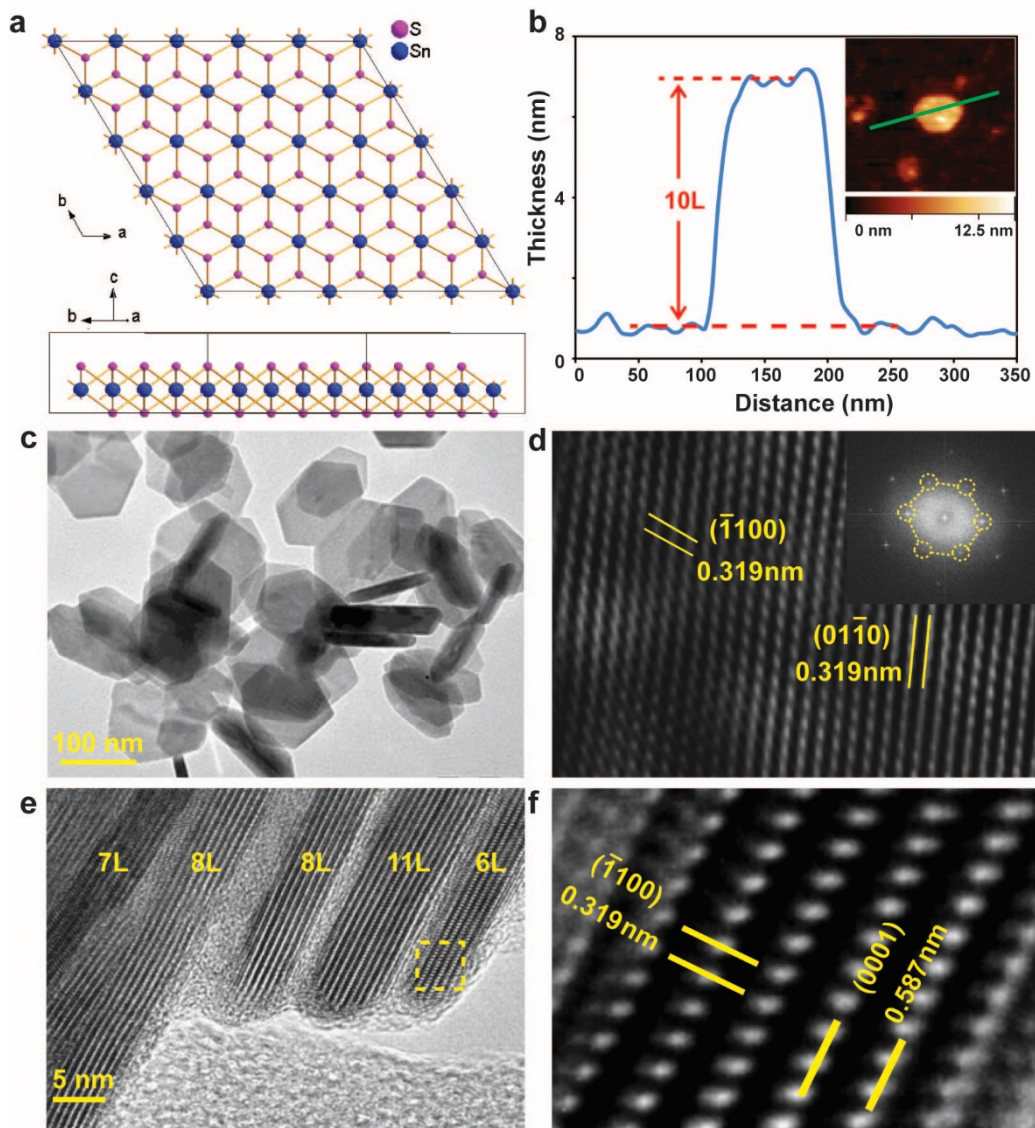
40. Ahn, J.-H.; Lee, M.-J.; Heo, H.; Sung, J. H.; Kim, K.; Hwang, H.; Jo, M.-H. Deterministic Two-Dimensional Polymorphism Growth of Hexagonal *n*-Type SnS<sub>2</sub> and Orthorhombic *p*-Type SnS Crystals. *Nano Lett.* 2015, 15, 3703-3708.
41. Su, G.; Hadjiev, V. G.; Loya, P. E.; Zhang, J.; Lei, S.; Maharjan, S.; Dong, P.; M. Ajayan, P.; Lou, J.; Peng, H. Chemical Vapor Deposition of Thin Crystals of Layered Semiconductor SnS<sub>2</sub> for Fast Photodetection Application. *Nano Lett.* 2015, 15, 506-513.
42. Du, Y.; Yin, Z.; Rui, X.; Zeng, Z.; Wu, X.-J.; Liu, J.; Zhu, Y.; Zhu, J.; Huang, X.; Yan, Q., *et al.* A Facile, Relative Green, and Inexpensive Synthetic Approach toward Large-Scale Production of SnS<sub>2</sub> Nanoplates for High-Performance Lithium-Ion Batteries. *Nanoscale* 2013, 5, 1456-1459.
43. Kim, T.-J.; Kim, C.; Son, D.; Choi, M.; Park, B. Novel SnS<sub>2</sub>-Nanosheet Anodes for Lithium-Ion Batteries. *J. Power Sources* 2007, 167, 529-535.
44. Seo, J.-w.; Jang, J.-t.; Park, S.-w.; Kim, C.; Park, B.; Cheon, J. Two-Dimensional SnS<sub>2</sub> Nanoplates with Extraordinary High Discharge Capacity for Lithium Ion Batteries. *Adv. Mater.* 2008, 20, 4269-4273.
45. Zhang, Y. C.; Du, Z. N.; Li, S. Y.; Zhang, M. Novel Synthesis and High Visible Light Photocatalytic Activity of SnS<sub>2</sub> Nanoflakes from SnCl<sub>2</sub>·2H<sub>2</sub>O and S Powders. *Appl. Catal. B-Environ* 2010, 95, 153-159.
46. Björkman, T.; Gulans, A.; Krasheninnikov, A. V.; Nieminen, R. M. Van Der Waals Bonding in Layered Compounds from Advanced Density-Functional First-Principles Calculations. *Phys. Rev. Lett.* 2012, 108, 235502.
47. Smith, A. J.; Meek, P. E.; Liang, W. Y. Raman Scattering Studies of SnS<sub>2</sub> and SnSe<sub>2</sub>. *J. Phys. C Solid State* 1977, 10, 1321.

48. Chandrasekhar, H. R.; Humphreys, R. G.; Zwick, U.; Cardona, M. Infrared and Raman Spectra of the IV-VI Compounds SnS and SnSe. *Phys. Rev. B* 1977, 15, 2177-2183.
49. Price, L. S.; Parkin, I. P.; Hardy, A. M. E.; Clark, R. J. H.; Hibbert, T. G.; Molloy, K. C. Atmospheric Pressure Chemical Vapor Deposition of Tin Sulfides (SnS, Sn<sub>2</sub>S<sub>3</sub>, and SnS<sub>2</sub>) on Glass. *Chem. Mater.* 1999, 11, 1792-1799.
50. Seminovski, Y.; Palacios, P.; Wahnón, P. Effect of Van Der Waals Interaction on the Properties of SnS<sub>2</sub> Layered Semiconductor. *Thin Solid Films* 2013, 535, 387-389.
51. Domingo, G.; Itoga, R. S.; Kannewurf, C. R. Fundamental Optical Absorption in SnS<sub>2</sub> and SnSe<sub>2</sub>. *Phys. Rev.* 1966, 143, 536-541.
52. Faglia, G.; Baratto, C.; Sberveglieri, G.; Zha, M.; Zappettini, A. Adsorption Effects of NO<sub>2</sub> at ppm Level on Visible Photoluminescence Response of SnO<sub>2</sub> Nanobelts. *App. Phys. Lett.* 2005, 86, 011923.
53. Shibata, T.; Kambe, N.; Muranushi, Y.; Miura, T.; Kishi, T. Optical Characterisation of Single Crystal 2H-SnS<sub>2</sub> Synthesised by the Chemical Vapour Transport Method at Low Temperatures. *J. Phys. D Appl. Phys.* 1990, 23, 719.
54. Deshpande, N. G.; Sagade, A. A.; Gudage, Y. G.; Lokhande, C. D.; Sharma, R. Growth and Characterization of Tin Disulfide (SnS<sub>2</sub>) Thin Film Deposited by Successive Ionic Layer Adsorption and Reaction (SILAR) Technique. *J. Alloy Comd.* 2007, 436, 421-426.
55. NIOSH. NIOSH Pocket Guide to Chemical Hazards. <http://www.cdc.gov/niosh/npg/npgd0454.html> (accessed 23/09/2015).
56. Shi, W.; Huo, L.; Wang, H.; Zhang, H.; Yang, J.; Wei, P. Hydrothermal Growth and Gas Sensing Property of Flower-Shaped SnS<sub>2</sub> Nanostructures. *Nanotechnology* 2006, 17, 2918.
57. Zhao, S.; Xue, J.; Kang, W. Gas Adsorption on MoS<sub>2</sub> Monolayer from First-Principles Calculations. *Chem. Phys. Lett.* 2014, 595–596, 35-42.

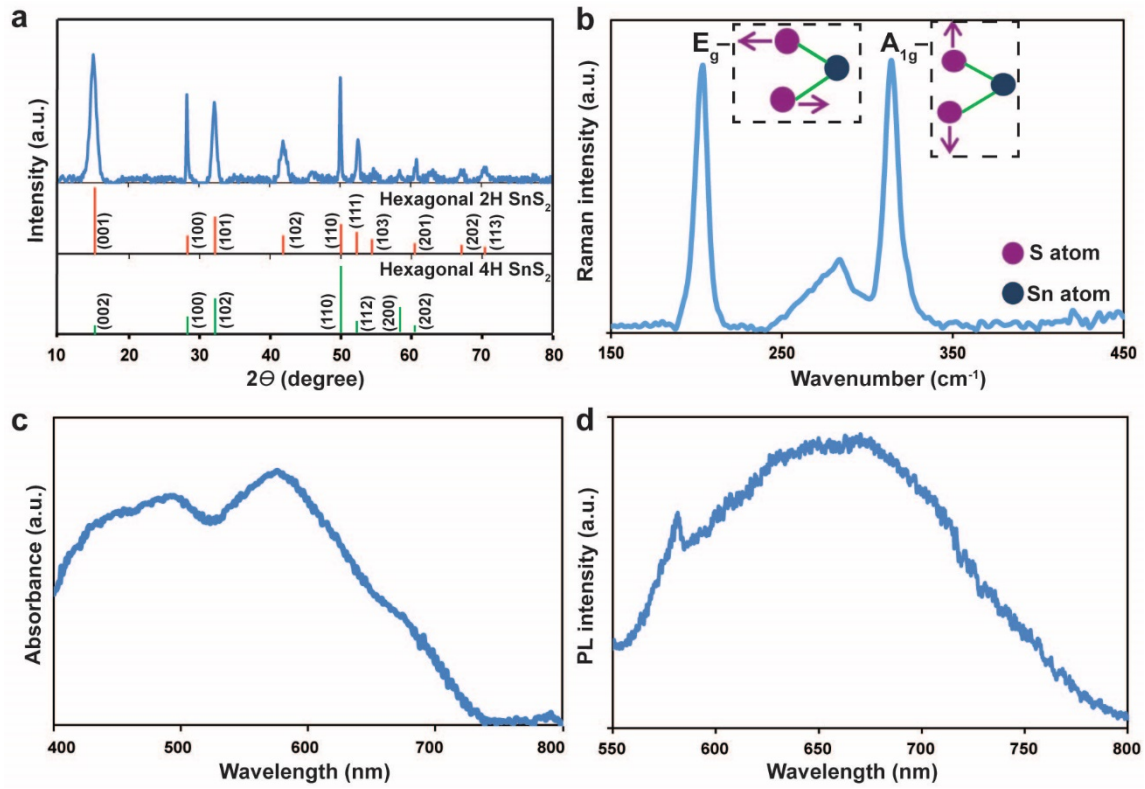


58. Liu, J.; Li, Q.; Zou, Y.; Qian, Q.; Jin, Y.; Li, G.; Jiang, K.; Fan, S. The Dependence of Graphene Raman D-Band on Carrier Density. *Nano Lett.* 2013, 13, 6170-6175.
59. Rakesh, V.; Barun, D.; Chandra Sekhar, R.; Rao, C. N. R. Effects of Charge Transfer Interaction of Graphene with Electron Donor and Acceptor Molecules Examined Using Raman Spectroscopy and Cognate Techniques. *J. Phys. Condens. Mat.* 2008, 20, 472204.
60. Shi, Y.; Huang, J.-K.; Jin, L.; Hsu, Y.-T.; Yu, S. F.; Li, L.-J.; Yang, H. Y. Selective Decoration of Au Nanoparticles on Monolayer MoS<sub>2</sub> Single Crystals. *Sci. Rep.* 2013, 3, 1839.
61. Yuan, J.; Najmaei, S.; Zhang, Z.; Zhang, J.; Lei, S.; M. Ajayan, P.; Yakobson, B. I.; Lou, J. Photoluminescence Quenching and Charge Transfer in Artificial Heterostacks of Monolayer Transition Metal Dichalcogenides and Few-Layer Black Phosphorus. *ACS Nano* 2015, 9, 555-563.
62. Newaz, A. K. M.; Prasai, D.; Ziegler, J. I.; Caudel, D.; Robinson, S.; Haglund Jr, R. F.; Bolotin, K. I. Electrical Control of Optical Properties of Monolayer MoS<sub>2</sub>. *Solid State Commun.* 2013, 155, 49-52.
63. Al Ashry, H. S.; Modrykamien, A. M. Humidification during Mechanical Ventilation in the Adult Patient. *BioMed Res. Int.* 2014, 2014, 12.
64. Kacmarek, R. M.; Stoller, J. K.; Heuer, A. *Egan's Fundamentals of Respiratory Care.* Elsevier: 2013.
65. Dovesi, R.; Orlando, R.; Erba, A.; Zicovich-Wilson, C. M.; Civalleri, B.; Casassa, S.; Maschio, L.; Ferrabone, M.; De La Pierre, M.; D'Arco, P., *et al.* CRYSTAL14: A Program for the *Ab Initio* Investigation of Crystalline Solids. *Int. J. Quantum Chem.* 2014, 114, 1287-1317.
66. Dovesi, R.; Saunders, V. R.; Roetti, C.; Orlando, R.; Zicovich-Wilson, C. M.; Pascale, F.; Civalleri, B.; Doll, K.; Harrison, N. M.; Bush, I. J., *et al.* *CRYSTAL14 User's Manual* University of Torino: Torino, 2014.

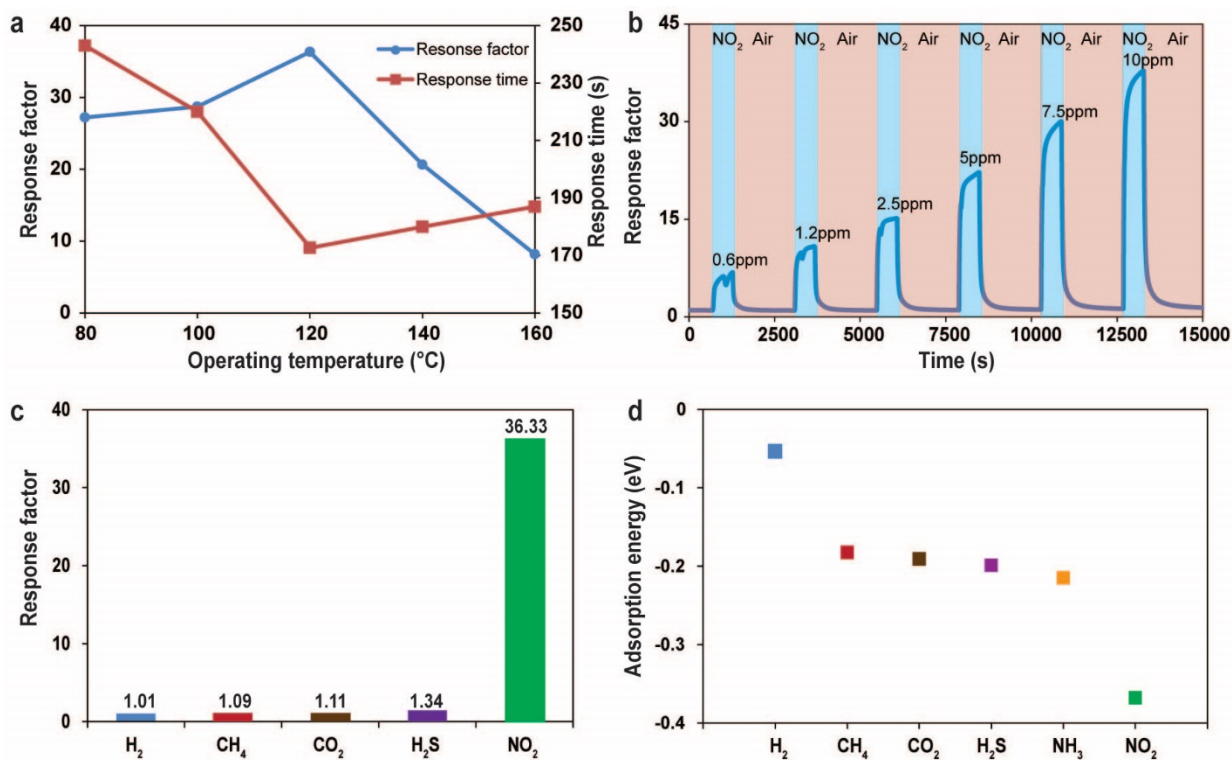
67. Becke, A. D. Density-Functional Thermochemistry. III. The Role of Exact Exchange. *J. Chem. Phys.* 1993, 98, 5648-5652.
68. Grimme, S. Semiempirical GGA-Type Density Functional Constructed with A Long-Range Dispersion Correction. *J. Comput. Chem.* 2006, 27, 1787-1799.
69. Civalleri, B.; Zicovich-Wilson, C. M.; Valenzano, L.; Ugliengo, P. B3LYP Augmented with An Empirical Dispersion Term (B3LYP-D\*) as Applied to Molecular Crystals. *CrystEngComm* 2008, 10, 405-410.
70. Peintinger, M. F.; Oliveira, D. V.; Bredow, T. Consistent Gaussian Basis Sets of Triple-Zeta Valence with Polarization Quality for Solid-State Calculations. *J. Comput. Chem.* 2013, 34, 451-459.
71. Crystal - Basis Sets Library. <http://www.crystal.unito.it/basis-sets.php>.



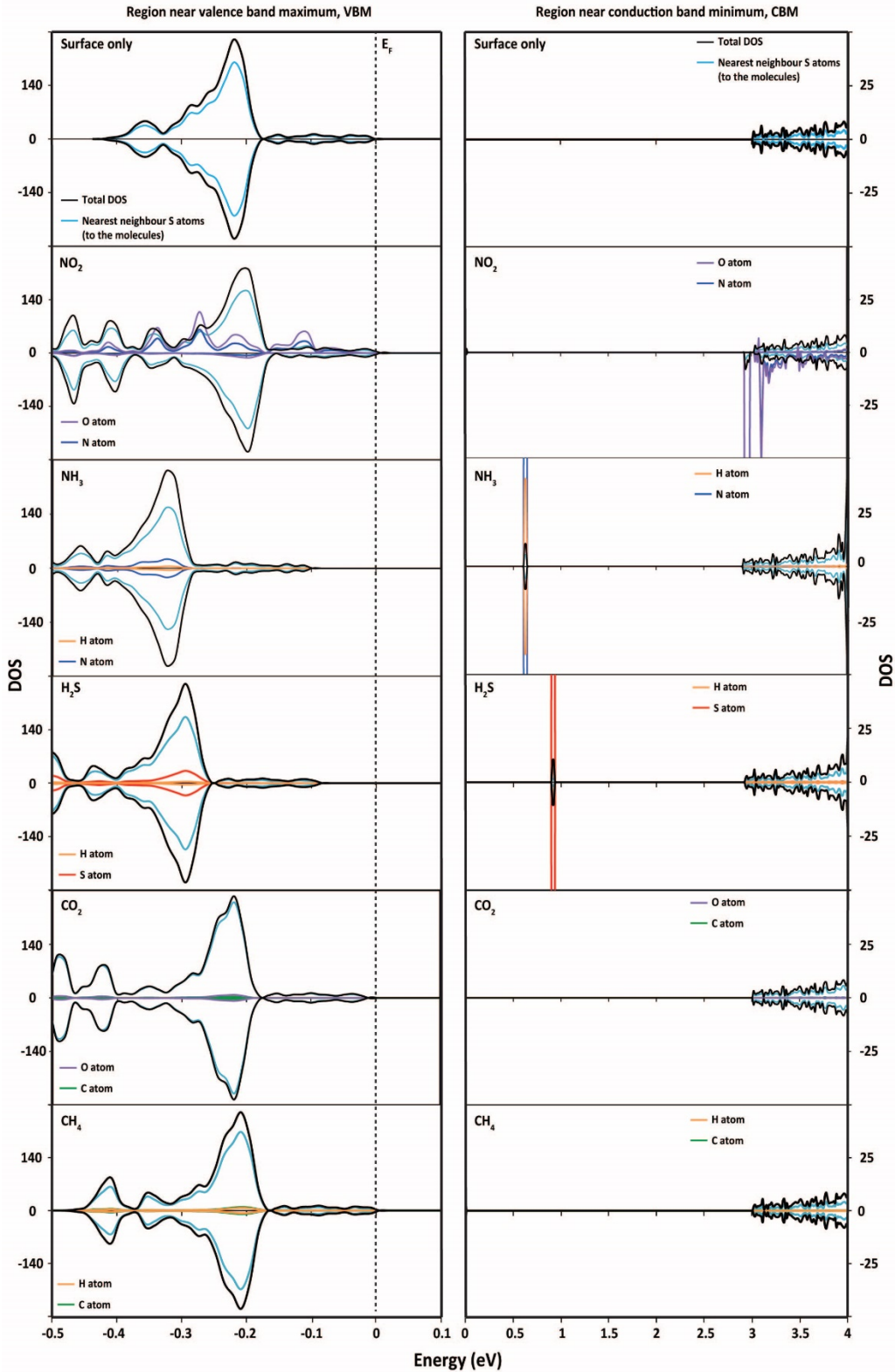
**Figure 1. Morphological and structural characterization of 2D SnS<sub>2</sub> flakes.** **a.** Top and cross-sectional schematics of SnS<sub>2</sub>; **b.** Height profile of a typical 2D SnS<sub>2</sub> flake along the green line in the AFM image inset; **c.** TEM image of 2D SnS<sub>2</sub> flakes; **d.** HRTEM image of a typical 2D SnS<sub>2</sub> flake; **e.** Cross-sectional HRTEM of 2D SnS<sub>2</sub> flakes; **f.** The zoomed in HRTEM figure indicating the interlayer spacing for hexagonal SnS<sub>2</sub> is 0.587 nm.



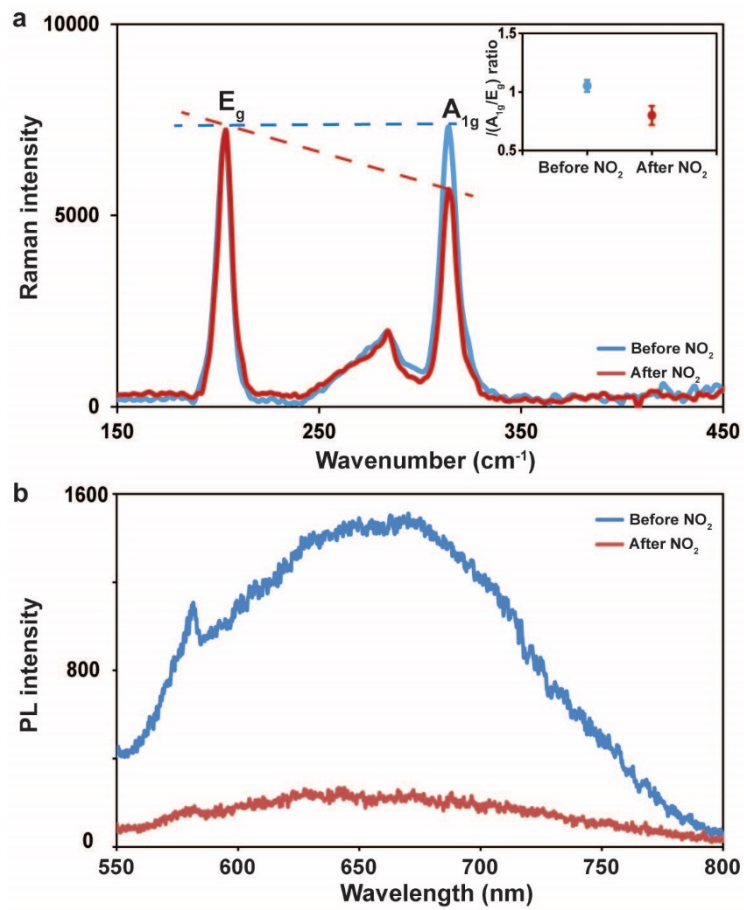
**Figure 2. Crystal structure and optical properties of 2D SnS<sub>2</sub> flakes.** **a.** XRD pattern of 2D SnS<sub>2</sub> flakes; **b.** Raman spectrum of 2D SnS<sub>2</sub> flakes at the laser excitation wavelength of 785 nm with schematics of  $E_g$  and  $A_{1g}$  Raman vibrational modes; **c.** The optical absorption spectrum of 2D flakes at the wavelengths between 400 to 800 nm; **d.** The PL spectrum of 2D flakes at the excitation wavelength of 532 nm.



**Figure 3. Gas sensing performance of 2D SnS<sub>2</sub> flakes.** **a.** Response factor and response time of sensors made of 2D SnS<sub>2</sub> flakes in the presence of 10 ppm NO<sub>2</sub> in synthetic air balance as a function of operation temperatures; **b.** Dynamic sensing performance of 2D SnS<sub>2</sub> flakes toward NO<sub>2</sub> gas at the concentrations ranged from 0.6 to 10 ppm under the operation temperature of 120°C; **c.** Measured cross-talk of 2D SnS<sub>2</sub> flakes towards H<sub>2</sub> (1%), CH<sub>4</sub> (10%), CO<sub>2</sub> (10%), H<sub>2</sub>S (56 ppm) and NO<sub>2</sub> (10 ppm); **d.** Calculated molecule-surface adsorption energies of 2D SnS<sub>2</sub> flakes towards the aforementioned gases together with NH<sub>3</sub>.

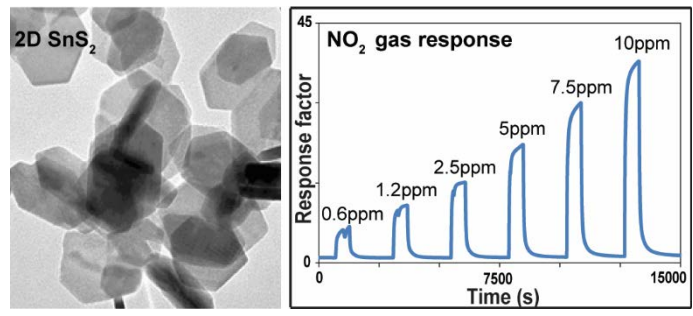


**Figure 4.** eDOS of  $\text{NO}_2$ ,  $\text{NH}_3$ ,  $\text{H}_2\text{S}$ ,  $\text{CO}_2$  and  $\text{CH}_4$  adsorbed on  $\text{SnS}_2$  in a  $5 \times 5 \times 1$  supercell, in which the clean surface of  $\text{SnS}_2$  is utilized as the reference. The Fermi level (0 eV along the energy scale) is aligned to that of  $\text{SnS}_2$  clean surface ( $E_F$ ) and the total eDOS is also scaled, so that the shape of the DOS can be visible on the same axis as the projected eDOS results.



**Figure 5. Physisorption based charge transfer in 2D SnS<sub>2</sub> flakes upon NO<sub>2</sub> gas exposure. a.** Raman spectra of 2D SnS<sub>2</sub> flakes before and after NO<sub>2</sub> gas exposure at 120°C. The corresponding intensity ratio of A<sub>1g</sub> and E<sub>g</sub> modes is shown in the inset. The error bar represents the standard deviation based on the analysis of 100 samples; **b.** PL spectra of 2D SnS<sub>2</sub> flakes before and after NO<sub>2</sub> gas exposure at 120°C.





ToC Figure